TECHNICAL ARTICLE

A novel immune competent murine hypertrophic scar contracture model: A tool to elucidate disease mechanism and develop new therapies

Mohamed Magdy Ibrahim, MD[1]; Jennifer Bond, PhD[1]; Andrew Bergeron, BA[1]; Kyle J. Miller, BA[1]; Tosan Ehanire, BA[1]; Carlos Quiles, MD[1]; Elizabeth R. Lorden, MS[3]; Manuel A. Medina, MD[1]; Mark Fisher, MD[1]; Bruce Klitzman, PhD[1,3]; M. Angelica Selim, MD[2]; Kam W. Leong, PhD[3]; Howard Levinson, MD[1,2]

1. Division of Plastic and Reconstructive Surgery, Department of Surgery,
2. Department of Pathology, Duke University School of Medicine, and
3. Department of Biomedical Engineering, Duke University, Durham, North Carolina

Reprint requests:
Dr. Howard Levinson, Division of Plastic and Reconstructive Surgery, Department of Surgery, Duke University School of Medicine, Durham, NC 27710, USA.
Tel: 9196848661;
Fax: 9196817340;
Email: howard.levinson@duke.edu

Manuscript received: October 18, 2013
Accepted in final form: September 4, 2014

DOI:10.1111/wrr.12238

ABSTRACT

Hypertrophic scar (HSc) contraction following burn injury causes contractures. Contractures are painful and disfiguring. Current therapies are marginally effective. To study pathogenesis and develop new therapies, a murine model is needed. We have created a validated immune-competent murine HSc model. A third-degree burn was created on dorsum of C57BL/6 mice. Three days postburn, tissue was excised and grafted with ear skin. Graft contraction was analyzed and tissue harvested on different time points. Outcomes were compared with human condition to validate the model. To confirm graft survival, green fluorescent protein (GFP) mice were used, and histologic analysis was performed to differentiate between ear and back skin. Role of panniculus carnosus in contraction was analyzed. Cellularity was assessed with 4′,6-diamidino-2-phenylindole. Collagen maturation was assessed with Picrosirius red. Mast cells were stained with Toluidine blue. Macrophages were detected with F4/80 immune. Vascularity was assessed with CD31 immune. RNA for contractile proteins was detected by quantitative real-time polymerase chain reaction (qRT-PCR). Elastic moduli of skin and scar tissue were analyzed using a microstrain analyzer. Grafts contracted to ~45% of their original size by day 14 and maintained their size. Grafting of GFP mouse skin onto wild-type mice, and analysis of dermal thickness and hair follicle density, confirmed graft survival. Interestingly, hair follicles disappeared after grafting and regenerated in ear skin configuration by day 30. Radiological analysis revealed that panniculus carnosus doesn't contribute to contraction. Microscopic analyses showed that grafts show increase in cellularity. Granulation tissue formed after day 3. Collagen analysis revealed increases in collagen maturation over time. CD31 stain revealed increased vascularity. Macrophages and mast cells were increased. qRT-PCR showed up-regulation of transforming growth factor beta, alpha smooth muscle actin, and rho-associated protein kinase 2 in HSc. Tensile testing revealed that human skin and scar tissues are tougher than mouse skin and scar tissues.

ASMA	Alpha smooth muscle actin	MSA	Microstrain analyzer
DAPI	4′,6-diamidino-2-phenylindole	NMMII	Nonmuscle myosin II
ECM	Extracellular matrix	PC	Panniculus carnosus
GFP	Green fluorescent protein	qRT-PCR	Quantitative real-time polymerase chain reaction
HPF	High-power field	ROCK2	Rho-associated protein kinase
IACUC	Institutional animal care and use committee	STSG	Split thickness skin graft
IGF-1	Insulin-like growth factor 1	TGF-β	Transforming growth factor beta
MLCK	Myosin-light-chain kinase	WT	Wild-type

Dermal scarring affects more than 100 million people worldwide annually.[1] Over 2.4 million Americans suffer from burns each year, and 2 million people are injured in motor vehicle accidents.[2] Burn wounds cost billions of dollars per year worldwide.[3] Burn wounds often heal by forming hypertrophic scars (HSc). HScs are firm, raised, red, itchy scars that develop over 6 months to 2 years. They are disfiguring and can have a severe impact on quality of life.[4,5] HSc contract, and when contraction occurs across a joint, it restricts range-of-motion, resulting in a scar contracture. HSc contractures are estimated to occur in up to 40% of major burn patients in the United States, and in patients who develop contractures at least four corrective surgeries are required on average.[6] There are presently no effective therapies to prevent HSc contractures.[4]

Third-degree burns extend completely through the dermis and are managed by excision of burned tissue and subsequent skin grafting, usually 3 days after excision. Skin graft survival consists of several stages. During the first 48 hours after placement, the skin graft is ischemic and depends upon diffusion of nutrients and dissolved oxygen from the underlying wound/granulation bed, a process called plasmatic imbibition.[7] Subsequently, blood vessels from the granulation bed invade the skin graft to deliver nourishment and remove wastes via a process called inosculation.[8] Inflammatory cells, including macrophages, invade the granulation bed as the graft continues to mature. Macrophages have a large influence on scarring by removing debris and pathogens, and secreting pro-healing cytokines and growth factors.[9] By the third post-operative day, blood flow is established through these anastomotic connections, and fibroblasts have begun to migrate in from the surrounding tissue, first into the granulation tissue of the wound bed and subsequently into the skin graft.[10] During this process, fibroblasts begin to differentiate into myofibroblasts in the wound bed. This differentiation is driven by the transmission of mechanical stress, along with immune-mediated release of soluble factors, such as transforming growth factor beta (TGF-β). Myofibroblasts lay down extracellular matrix (ECM) components which replace the provisional matrix and also exhibit contractile properties due to the expression of alpha smooth muscle actin (ASMA) in actin stress fibers.[11] ASMA enhances the cell's contractile abilities, and plays a significant role in wound contraction and granulation tissue maturation.[12] Once wound contraction and healing are complete, myofibroblasts should resolve by apoptosis. A lack of myofibroblast apoptosis is thought to promote HSc.[12]

Despite the significance of HSc contractures, preclinical investigations into the pathogenesis of HSc contraction and development of new therapies to prevent HSc contraction are lacking. One of the major hurdles to developing an effective HSc therapy is the lack of an immune-competent murine model.[5] Human HSc has typically been studied in immune-compromised mice, in which multiple models have been developed. In 1989, human HScs were transplanted into subcutaneous pockets of athymic mice.[13] The partially revascularized, ischemic, transplanted scars were considered to represent human scar tissue, but in fact they only comprised the terminal stages of scarring and did not contain the initiating factors that led to development of the disease. In 2004, a mouse model with genetically modified skin-humanized mice was introduced.[14] Cultured human keratinocytes were transfected with an enhanced green fluorescent protein (GFP) retroviral vector and transplanted on the back of nude mice.[14] However, this model was designed to mimic excisional wounds in healthy human volunteers, not larger-size wounds requiring skin grafts and/or dermal substitutes. In 1987, an HSc murine model was introduced, whereby full thickness human skin grafts were transplanted onto the backs of nude mice and subsequently burned.[15] This study was repeated in 2007 by another group that observed similar HSc formation without the burning step. These mice developed raised, red, itchy, firm HSc that histologically resembled human HSc. The HSc was prominent after 1–3 months, and subsequently diminished after 6 months.[16] Although the progressive development of improved "humanized" mouse models has resulted in a greater understanding of human HSc tissue in vivo, none of these models possess an intact immune system. The established importance of immunity in the process of HSc formation reveals a major weakness in the ability of these models to adequately model the disease conditions.[17] In 2007, Gurtner et al. developed a mechanical model of HSc in immune-competent mice.[18] The ensuing HSc showed many histopathological similarities to human HSc.[18] While this model provides a strategy to circumvent utilizing immune-compromised animals, it does not recapitulate the present conditions in most burn scar injuries. Therefore, the purpose of this study was to develop a novel immune-competent murine HSc contraction model that possesses all of the advantages of murine models with an abundance of genetic variants and applicable tools, low purchase, and housing costs. The goal of this work is that this model will serve to advance the field of wound healing and scarring.

MATERIALS AND METHODS

Mice

Female C57BL/6 mice, 10–12 weeks old, weighing 18 to 23 g (Jackson Laboratories, Bar Harbor, ME), were used as wild-type (WT) mice throughout the study. Female hemizygous C57BL/6-Tg(CAG-EGFP)131Osb/LeySopJ carriers (GFP) and noncarrier control littermates, 10–12 weeks-old, weighing 18 to 23 g (Jackson Laboratories) were used for WT-GFP and GFP-WT studies. All mice were monitored for signs of toxicity, including changes in: weight, grooming, irritability, and respiratory rate. The mice were housed under protocols approved by the Institutional Animal Care and Use Committee (IACUC) of Duke University.

Producing a third-degree thermal injury

All procedures were performed in accordance with a protocol approved by the Duke University IACUC. Mice were anesthetized using gas anesthesia (oxygen, 2 L/min, isoflurane, 2%). The recipient mouse was anesthetized and the back of the mouse was shaved with metallic clippers. The back was then sterilized using alcohol. The mouse was placed in a restraining tube. A metal brass rod 8 mm in diameter, weighing 65 g, was placed in boiling water for 15 minutes; the brass rod was confirmed to be 100 °C. The surface of the brass rod was wiped dry and then placed on the back of the mouse for 1 second to produce a third-degree burn. The burn was left for 3 days, and a 14-mm diameter circle over the burn site was excised for recipient skin grafting.

Skin transplantation

The donor mouse was anesthetized. Its ears were cleansed with alcohol and cut at the base with curved surgical scissors. The dorsal skin surface of the ear was carefully separated from the cartilaginous ventral surface using sharp, fine-tipped scissors, and the cartilaginous surface was discarded. Three fenestrations were created in the dorsal ear skin using a #10 scalpel, 2 mm apart.Two donor skin ears were laid over an excised 14-mm diameter burn wound. The edges of the grafts and the edges of the skin were approximated and sutured with interrupted stitches (five stitches for each ear and two stitches between the two ears) using 6-0 silk suture. The skin grafts were then secured with a padded bolster. The bolster was removed on postoperative day 3.

Tagging the panniculus carnosus (PC)

The PC muscle layer around the skin graft was identified and excised, and the margins were tagged with six surgical titanium micro clips (Microclip, Teleflex Medical, Research Triangle Park, NC) in a circular arrangement. X-ray images were captured using an x-ray device (Faxitron Bioptics, Tucson, AZ). The mice were placed with the skin graft in the central gridline of the device. The x-ray images were captured on days 3, 10, 17, and 24 postsurgery. The surface area surrounded by the titanium clips was measured using ImageJ software (National Institutes of Health, Bethesda, MD).

Tissue collection

The mice were euthanized and tissue was collected on postoperative days 3, 7, 9, 11, 14, 28, 70, and 168. The collected tissues were cut into equal halves. One half was preserved in 10% formalin and paraffin embeded for histological analyses, while the other half was immediately frozen in liquid nitrogen for additional analyses. Prior to staining, tissue sections were de-paraffinized by warming at 65°C overnight, immersing in xylene for 15 minutes, rehydrating with decreasing concentrations of ethanolin distilled water.

Histology

Routine hematoxylin & eosin (H&E), 4′,6-diamidino-2-phenylindole (DAPI), Toluidine blue, and picrosirius red staining to enhance polarization of collagen fibers were performed on 5-μm-thick paraffin-embedded sections. For collagen index, the color information from each Masson trichrome high-power field (HPF) image was quantified using colorimetric analysis. The collagen index value was calculated as collagen index = (B + G) / (2R + B + G) for each pixel within the image (where R, G, and B represent the red, blue, and green pixel values, respectively). The value of the collagen index ranged from 0 for extremely red objects to 1 for completely blue-green objects. The average collagen index of three (HPF) images for each time point was graphed.

Immunohistological staining

Tissue sections were immersed in 3% hydrogen peroxide for 10 minutes to inhibit endogenous peroxidase. Slides were placed into citrate pH 6 antigen retrieval solution (Target Retrieval Solution, Dako North America Inc., Carpinteria, CA) and brought to >85°C in a water bath for 20 minutes, followed by a 30-minute cool down. After rinsing sections with deionized water and 1X Tris-buffered saline (TBS; TBS Automation Washing Buffer, Biocare Medical, Concord, CA), sections were treated with 10% goat serum (Normal Goat Serum S-1000, Vector Laboratories, Burlingame, CA) for 1 hour at room temperature to block nonspecific antibody binding.

Macrophage F4/80 staining

F4/80 (14–4801-83, 1:1500 dilution, eBioscience, San Diego, CA) was incubated for 1 hour at room temperature. After washing with TBS, the slides were incubated with biotinylated rabbit anti rat (BA-4000, 1:200 dilution, Vector Laboratories) for 30 minutes at room temperature.

Staining of endothelial cells for CD31

Anti-CD31 antibody (AB28364, 1:50 dilution, Abcam, Cambridge, MA) was incubated for 1 hour at room temperature. After washing with TBS, the slides were incubated with biotinylated goat anti-rabbit (BA-1000, 1:50 dilution, Vector Laboratories) for 30 minutes at room temperature.

Following incubation in secondary antibodies, the sections were then incubated with avidin-biotin complex reaction (PK-7100, Vector Laboratories) for 30 minutes. The sections were incubated with DAB substrate solution (DBC859L10, Biocare Medical) for 3 minutes after rinsing with 1X TBS. The slides were quickly dipped in hematoxylin solution for counterstain solution, and then rinsed in running tap water for 20 minutes. After dehydration, labeled cells were visualized by use of a Nikon eclipse E600 microscope (Tokyo, Japan) and images were captured with a Nikon DXM 1200 digital camera under the same settings. Five HPF images were analyzed from each tissue section, and the average number of cells was assayed.

Quantitative real-time polymerase chain reaction (qRT-PCR)

Total RNA from was isolated using RNeasy Plus Universal Mini Kit (73404, Qiagen, Valencia, CA) including DNase treatment. Diluted by 10 mM Tris buffer, RNA concentration and purity of the samples were measured by use of spectrophotometer (Beckman Coulter, Brea, CA). Afterwards, following the standard one-step RT-PCR protocol for use with the QuantiTect SYBR Green RT-PCR Kit (204243, Qiagen) and Mx3005P QPCR System (Agilent Technologies Inc., Santa Clara, CA), template RNA (10 ng/reaction) was added to prepare reaction mix. The one-step PCR cycling conditions were: 50°C for 30 minutes, 95°C for 15 minutes, 40 cycles of 94°C for 15 seconds, 55°C for 30 seconds, and 72°C for 30 seconds. S9 was employed as a housekeeping gene. Data were collected and analyzed by MxPor QPCR software (Agilent Technologies Inc.); relative gene expression is calculated as a ratio of Ct of the interested gene to that of S9. All qRT-PCR primers were purchased from Qiagen.

Mechanical testing of tissue samples

Scar and uninjured skin samples were gathered from human and murine donors. Human skin samples were donated from discarded human tissue from Duke Hospital operating rooms under exemption by Duke Institutional Review Board (IRB). Uninjured skin was gathered from breast resection, while scar tissue was taken from excised keloid, radiated forearm, and rejected skin graft. Tissue from three human donors was used, with three to five biological replicates per donor. Uninjured murine tissue samples were collected from the dorsum of 10–12 week-old C57BL/6 mice. Murine scar tissue was taken from contracted day 28 skin-grafted mice. Tissue from five murine donors was used, with three biological replicates per donor. All human and murine tissues were kept moist on damp gauze between collection and mechanical testing, and analyzed within 1–5 hours of collection. Prior to testing, underlying tissue was removed and samples were cut into uniform strips. Elastic moduli of human and murine skin samples were analyzed using a microstrain analyzer (MSA) (TA Instruments RSA III, New Castle, DE). Samples were cut into strips 3 mm wide and 4 cm long, and loaded with a 5 mm gap between the grips. The samples were strained at a rate of 0.1 mm/second at room temperature (23°C) until failure. Many of the human skin samples overloaded the maximum force of the MSA (35 N) and had to be stopped prior to failure. Stress-strain curves were graphed in Excel, and the elastic modulus of the material (E) calculated as stress/strain (σ/ε) in the initial linear portion of the graph, prior to necking of the material.

Statistical analysis

Data were analyzed using Microsoft (Redmond, WA) Excel software. The statistical significance of values amonggroups was evaluated by the analysis of variance (ANOVA), followed by least significant difference *t*-test. All values used in figures and text are expressed as mean ± standard error of the mean (SEM). The difference was considered significant when the *p*-value was 0.05 or less.

RESULTS

Establishing a third-degree burn murine model

A third-degree burn injures the full thickness of the skin: the epidermis and the dermis.[19] Histological analysis revealed that a 1-second burn contact time with a 65 g brass rod heated to 100 °C, held in place by gravity, resulted in a reproducible full-thickness burn (Figure 1A). As is noted in the figure, there was necrosis throughout the epidermis and dermis, but not into the deep muscular layer.

Skin graft survival

Both donor and recipient mice were immune competent. This was intentionally done so that one could study the immune system as it relates to HSc and skin graft survival. The burned tissue of the recipient mouse was excised after 3 days and skin grafted to mimic clinical practice. Mouse ear skin was used as a donor for the skin graft (Figure 1B) and was transplanted onto the granulation tissue bed. During optimization of the model, we tested alternative skin donor sites, including murine back skin, tail skin, and abdominal skin, but had poor success due to the thickness of the skin graft. We attempted split-thickness skin graft harvesting utilizing a dermatome, but found the harvested layers to be inconsistent in quality and thickness. A bolster as a dressing for the split thickness skin graft (STSG) was necessary for STSG survival as an adhesive bandage was not reliable.

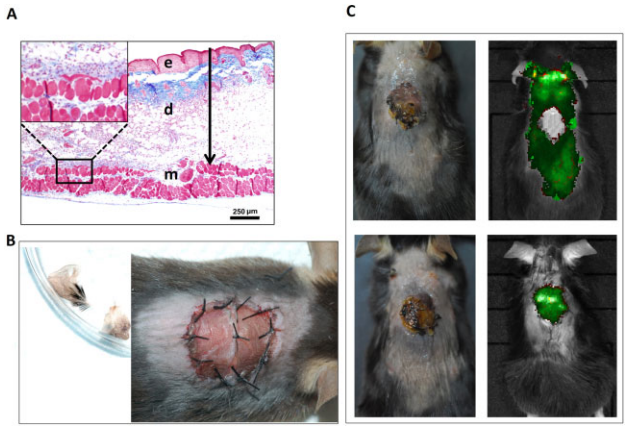

Figure 1. Third-degree burn injury model and skin graft survival. (A) Masson's trichrome staining of mouse skin revealed a third-degree burn (e, epidermis; d, dermis; m, muscle; black arrow, third-degree burn). Magnified section shows intact muscular layer. (B) Representative photographs of the dorsal ear skin graft before and after transplantation on the dorsum of the rodent. (C) Top row: donor ears were obtained from C57BL/6 mice and were grafted on GFP transgenic mice. Bottom row: donor ears were obtained from GFP transgenic mice and were grafted onto C57BL/6 mice. Mice were photographed under normal light (left) and the same mice were photographed under GFP excitation light demonstrating graft survival. GFP, green fluorescent protein.

To confirm the survival of the skin graft, we used GFP mice in two experiments. We used donor ear skin from a WT mouse and transplanted it to a GFP recipient mouse. The recipient GFP mouse appeared green while the transplanted WT skin graft appeared gray, indicating skin graft survival. We also used donor ear skin from a GFP mouse and transplanted it onto a WT recipient mouse. The recipient WT mouse appeared gray while the transplanted GFP skin graft appeared green, confirming skin graft survival (Figure 1C). Analysis was done on Day 30.

Mature skin grafts had the same dermal thickness and number of hair follicles as ear skin

To further confirm that we were observing skin graft survival and not traditional wound healing, we performed H&E analysis over a period of 6 months. Our analysis of dermal thickness showed that mature skin graft had the same dermal thickness as normal ear skin, ~90 µm. We also found that the number and frequency of hair follicles (Figure 2A) in mature skin graft correspond to normal ear skin. This confirmed that

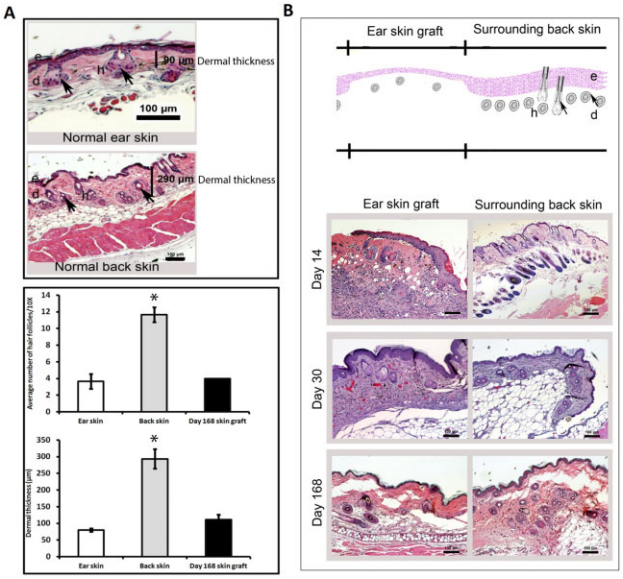

Figure 2. Skin graft survival. (A) H&E stained sections showing dermal thickness and density and number of hair follicles (h) per unit area in normal ear skin and normal back skin. The average number of hair follicles/field is graphically represented in normal ear skin, normal back skin, and day 168 skin graft. Mature skin grafts have the same number of hair follicles and same average dermal thickness as normal ear skin, indicating the ear skin grafts persist. (B) The hair follicles were absent in the early time points of the skin grafts, then hair follicles have regenerated again starting by day 30. d, dermis, e, epidermis. *, statistical significance.

the skin graft survived as donor ear skin and was not replaced by fibrous tissue or back skin (Figure 2A).

Interestingly, our analysis also revealed that the hair follicles disappeared in the early time point of skin graft survival, only to reappear again later on day 30 (Figure 2B).

Skin grafts contracted but did not disappear; PC did not contribute to skin graft contraction

Our macroscopic observation and measurement of skin graft size showed that the grafts contracted to ~45% of the original wound size by day 14, after which no further contraction was observed. In comparison, nongrafted wounds fully contracted by day 14 (Figure 3A). Grafts were initially red and flat, in contrast to the raised nature of early human HSc. However, human HSc often flatten as they mature (Figure 3B).

Rodents possess a subcutaneous muscle layer called the PC. The PC has been shown to promote wound contraction and thus expedite scar contraction.[20] Our radiological analysis on postoperative days 3, 10, 17, and 24 showed no significant change in the surface area of PC underneath the skin graft, indicating that the PC did not contribute to skin graft contraction (Figure 3C).

Skin grafts showed an increase in cellularity and granulation tissue formation

Histological analysis of DAPI-stained sections revealed significant increases in cellularity at all time points compared

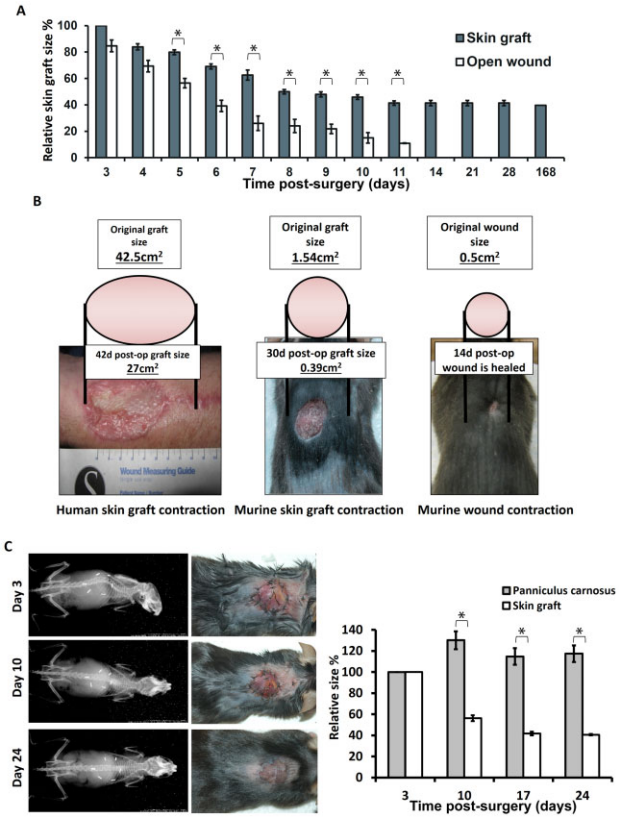

Figure 3. Skin graft contraction. (A) Graph showing the relative skin graft size vs. the relative open wound size, indicating that rodent skin grafts behave like human skin grafts. Open wounds were contracted and closed by day 14, whereas skin grafts stopped contraction by day 14 and remained 50% of the initial graft size. (B) The murine burn contracture model is analogous to the human condition with faster graft contraction: human skin grafts contract ~35% by 6 weeks, the murine skin graft contracts to ~45% of the original size by 4 weeks, and the murine open nongrafted wound contracts ~95% by 14 days. Note that contracted skin grafts are hypertrophic scars, but this does not mean that contracted hypertrophic scars are elevated. (C) Graph showing no significant change in the panniculus carnosus size at different time points, whereas the skin graft contracted to ~45% of the original size; these data show that the panniculus carnosus does not play a role in skin graft contraction in this model. *, statistical significance.

with normal mouse skin (Figure 4A). There was also a significant increase in granulation tissue surface area at all time points compared with normal mouse skin (Figure 4B).

Collagen maturation has increased over time

Picrosirius red analysis showed increase in collagen maturation over time; there were more immature (green, loosely packed) collagen fibers on day 7 than on day 21 and day 168. More mature collagen fibers (yellow, densely packed) were present on day 168 than on day 21 and day 7 (Figure 4D).

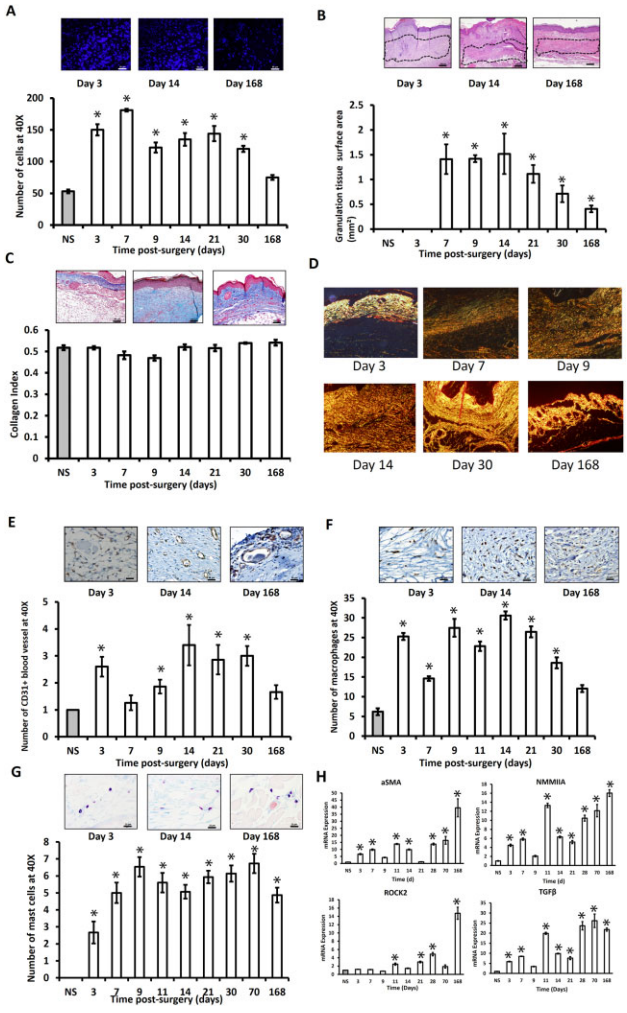

Figure 4. (A) Representative DAPI-stained section. All time points showed more cellularity than the normal skin. Day 7 showed the highest cellularity, whereas day 168 showed the least. (B) Representative H&E-stained sections. Granulation tissue surface area is graphically represented. Day 14 showed the greatest surface area of granulation tissue, then it decreased gradually up to day 168. (C) Representative Masson's trichrome-stained sections demonstrating collagen content of the skin grafts. Quantitative analysis of collagen index was graphically represented vs. normal skin. (D) Sirius red polarization microscopy of collagen fibers revealed an increase in collagen maturation over time. There were more immature (green, loosely packed) collagen fibers on day 7 than day 21 and day 168, respectively. Whereas, there was more mature collagen fibers (yellow, densely packed) on day 168 than on day 21 and day 7, respectively. (E) Representative CD31-stained sections demonstrating the degree of vascularity. All time points show more vascularity compared with normal skin. Day 14 showed the highest vascularity, whereas day 7 showed the least. (F) Representative F4/80-stained section demonstrating the density of macrophages. All time points show more macrophages compared with normal skin. Day 14 showed the highest number of macrophages, whereas day 168 showed the least. (G) Representative Toluidine blue-stained sections demonstrating the density of mast cells. All time points showed more mast cells compared with normal skin. Day 9 showed the highest number of mast cells, whereas day 3 showed the least. (H) mRNA expression of ASMA, NMMIIA, ROCK2, and TGF-β was assessed by qRT-PCR. Gene expression is related to ribosomal protein S9 using the ΔΔCt method and then normalized to normal skin. Data are represented as mean ± SEM. ASMA, NMMIIA, and TGF-β show an increase in expression in the graft tissue peaking at day 168. ROCK2 has the greatest increases in expression at days 28 and 168. ASMA, alpha smooth muscle actin; NMMIIA, nonmuscle myosin II A; qRT-PCR, quantitative real-time polymerase chain reaction; ROCK2, rho-associated protein kinase; TGF-β, transforming growth factor beta. *, statistical significance.

Skin grafts showed an increase in the vascular density

Immunohistochemistry showed increased number of endothelial cells, vascular density, at all time points of the skin grafts compared with the normal skin (Figure 4E).

Skin grafts showed an increase in the numbers of macrophages and mast cells

Immunohistochemistry using F4/80 as a marker, showed wide areas of positive macrophage staining in the skin grafts, and quantification showed an increase in the number of macrophages at all the time points of the skin grafts compared with the normal skin (Figure 4F). Histological analysis of Toluidine blue-stained sections showed an increase in the number of mast cells at all time points in the skin grafts compared with normal skin (Figure 4G).

Up-regulated mRNA expression of TGF-β and cytoskeletal proteins in skin grafts

Transforming growth factor beta (TGF-β), alpha smooth muscle actin (ASMA), nonmuscle myosin II (NMMII) A, and rho-associated protein kinase (ROCK2) have all been reported to coordinately regulate the development of fibrotic conditions.[21] qRT-PCR analysis showed increase mRNA expression of TGF-β, ASMA, NMMIIA, and ROCK2 at all time points compared with normal skin. Surprisingly, day 168 skin graft showed the highest mRNA expression (Figure 4H).

Skin grafts showed the same elasticity as HSc when compared with normal skin

Prior microstrain analysis studies have been conducted on human and mouse tissue.[18,22] Most of these tests utilize a strain rate of several mm/min or above. The measured elastic moduli are highly dependent upon the strain rate because skin is a viscoelastic tissue.[22] We chose a smaller strain rate of 0.1 mm/second to better approximate the slow speed of contraction

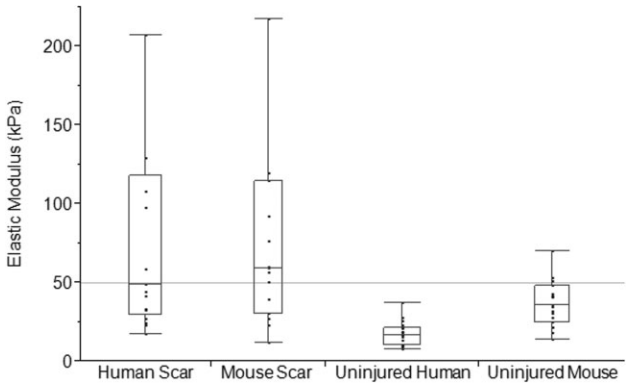

Figure 5. Comparison of measured elastic modulus between uninjured (normal) skin and scar tissue for human and mouse samples. Each marking represents a unique sample. Data are presented in this way to show variability of scar tissue and relative stiffness of human and mouse scars.

exerted by cellular forces on wounds. A comparison of elastic modulus between mouse scar, mouse normal skin, human scar, and human normal skin illustrated that mouse scar is stiff, akin to human scar, whereas unwounded mouse skin is more elastic like unwounded human skin (Figure 5).

Comparison of novel immune-competent murine hypertrophic scar contracture model as a hypertrophic scar model

Animal model validity is discussed in terms of similarities between the model and the human condition.[23] In humans, a third-degree burn injury is managed through excision of the dead tissue and delayed skin grafting.[24] The skin graft heals and contracts over 6 months. Our murine HSc contracture model shares many similarities with human HSc (Table 1).[25]

DISCUSSION

This study introduces a validated immune-competent murine HSc contraction model. First, a third-degree burn was created on the dorsum of a C57Bl/6 mouse. The burned tissue was subsequently excised, and a skin graft fashioned from donor murine ear skin was sutured over the wound. We initially secured the skin grafts with adhesive bandages, as described in transplant models, but this approach led to skin graft death. Murine ear skin, as opposed to skin from other donor sites such as murine flank, tail, or abdomen, was chosen due to the relative thinness of ear skin. Thin skin grafts were more likely to survive than thick skin grafts, and thin split thickness skin grafts are the preferred method of treatment in human burn wounds. Transplanted skin grafts showed viability at 2 weeks postoperation. Skin grafts contracted to ~45% of their original size in 2 weeks, as compared with excisional wounds which were contracted closed at 2 weeks postwounding. The rate of murine skin graft contraction was much faster than what is reported in human split thickness skin grafts of the scalp.[26] Over time, the murine skin grafts became flat and pale, as is observed in some, but not all human HSc.[27,28] The process of murine skin graft contraction showed many gross morphological and microscopic characteristics similar to human HSc (Table 1).[28]

The healing process following deep dermal injury is a stepwise sequence of overlapping events which often results in scar. Shortly after wounding, hemostasis is achieved and changes in blood vessel walls allow inflammatory cells to migrate into the wound. While inflammatory cells such as macrophages may appear 48 hours after wounding, prolonged inflammation is associated with skin fibrosis and HSc.[29] Macrophages, in particular, are a major source of cytokines and growth factors.[30] TGF-β is one such protein released by mac-

Table 1. Characteristics of human and murine hypertrophic scars

Parameter		Human HSc	Murine HSc
Initial injury	Burn	Third-degree burn	Third-degree burn
Management	Surgical	Excision and skin graft	Excision and skin graft
Gross appearance	Scar contraction	Increased	Increased
Matrix	Collagen maturation/type I	Increased	Increased
Cellularity	Vascularity	Increased	Increased
	Macrophage density	Increased	Increased
	Mast cell density	Increased	Increased
	Proliferation	Increased	Increased
Cytokines	TGF-β	Increased	Increased
Cytoskeletal changes	ASMA	Increased	Increased
	NMMIIA	Increased	Increased
	ROCK2	Increased	Increased
Elasticity	Elastic modulus	Increased compared with uninjured human skin	Increased compared with uninjured mouse skin

ASMA, alpha smooth muscle actin; HSc, hypertrophic scar contraction; NMMIIA, nonmuscle myosin II A; ROCK2, rho-associated protein kinase; TGF-β, transforming growth factor beta.

rophages that promotes HSc contraction and has been shown to be a potent chemotaxin for inflammatory cells, including macrophages and mast cells.[31] Dysfunction of normal macrophage response can result in numerous pathologic conditions, including ulcers, chronic wounds, keloids, and HSc.[31]

Mast cells are another type of inflammatory cell that participates in wound healing. As granulation tissue develops interstitial collagen, mast cells appear. It has been previously reported that HSc contains significantly greater numbers of mast cells than normal skin, and mast cells may be a stimulus for HSc contraction.[32] HSc contraction is caused by mast cells release of histamine and arachidonic acid metabolites, as well as angiotensin II.[33] Our group has previously demonstrated that increased levels of angiotensin II activate the contractile protein NMMIIA and promote dermal fibroblast contractility.[21]

As previously mentioned, increased vascular density has been observed in HSc. While the reason for increased vascularity is unclear, prior studies have suggested that increased vascularity could account for the persistent high inflammatory cell density observed in HSc.[25] Conversely, persistent inflammation could itself contribute to increased vascularity through positive feedback loops.[34] Our present study showed an increase in the vascularity of skin grafts compared with unwounded skin. Along with increased vascular density, we observed high concentrations of fibroblasts. Blood vessels and fibroblasts are the major constituents of a critically important transitional connective tissue called granulation tissue.[35] Granulation tissue may persist for up to 6.5 months postinjury, due to diminished cell apoptosis. This persistence of increased cell numbers contributes to HSc contraction because granulation tissue fibroblasts become aligned along lines of mechanical stress.[12,36]

Aligned fibroblasts differentiate into contractile and secretory myofibroblasts. Myofibroblasts lay down ECM and exhibit increased expression of ASMA in actin stress fibers.[11] Expression of ASMA in stress fibers confers at least a twofold stronger contractile activity to these specialized cells.[37] Myofibroblast cell contractility is regulated by myosin light-chain (MLC) phosphorylation in a manner similar to regulation of smooth muscle cell contraction.[38] Two kinase systems seem to regulate MLC phosphorylation: calcium (Ca^{2+})-dependent myosin-light-chain kinase (MLCK) and rho-kinase.[39] Myofibroblast contraction tends to be rapid and short-lived, as increases in intracellular $Ca^{2+}$are transient and active myosin phosphatase terminates the reaction by removing the phosphate group from MLC. In the rho kinase pathway, RhoA (a small Rho family GTPase) activates ROCK2.[40] Activated ROCK2 increases MLC phosphorylation by two mechanisms: first, by direct phosphorylation of MLC, and second, by inactivating myosin phosphatase through phosphorylation of the myosin-binding subunit.[41–43] Activated MLC binds to the neck domain of NMMII, which leads to NMMII sliding actin in a slip-ratchet fashion. Actomyosin contractility causes cell migration, adhesion, and contractility.[44] NMMII levels are increased under increased levels of matrix stiffness from collagen organization (such as scar tissue).[45]

Collagen organization plays a key role in the strength and elasticity of healthy skin and scar tissue.[46] In unwounded adult animals, collagen bundles are thick, arranged in a basketweave formation, and have a low index of organization. In HSc, collagen fibers are thin and arranged in parallel.[47] In our model, we observed an increase in immature collagen loosely packed in parallel fashion, with blood vessels perpendicular to the surface. These immature fibers gradually gave way to an abundance of mature, densely packed collagen fibers by day 168 (Figure 4D).

In HSc, the epidermal surface is devoid of appendages, such as hair follicles, and lacks the ingrowth of rete pegs.[48] Interestingly, in our model we noted the disappearance of hair follicles early after skin graft application, with later regeneration of hair follicles around day 30. The reappearance of hair follicles is unexpected, and suggests the possibility of cellular reprogramming or stem cell migration into the graft tissue.

Scar tissue exhibits different mechanical properties than unwounded tissue. HSc is less extensible, requires more energy to be stretched in the physiologic range, and stores strain energy less efficiently than unwounded skin.[22,49] Clark et al. demonstrated an up to seven times increase in stiffness in hypertrophic scars vs. normal skin tissue. Our results showed that scar tissue from our mouse model graft site was stiffer (79.46 ± 16.62 kPa) than unwounded mouse skin (36.41 ± 3.68 kPa). This relationship is similar to previously published findings and consistent with our findings in human tissue, with hypertrophic scars possessing an elastic modulus nearly three times as large as unwounded human skin (Figure 5).[18,22]

The lack of an ideal HSc contraction small animal model has greatly hindered both the understanding of this disease and the development of effective therapies for its prevention.[5,16,50] The mouse remains the most commonly used animal for biologic research, owing in large part to its ease of care, economic advantage, and wealth of mouse-specific reagents and genetic tools.[51] As previously mentioned, present murine models of HSc either lack an immune system or fail to effectively model the pathologic condition.[14–16,18,52] In addition to murine models, scientists have utilized other animals to study HSc. An athymic rat model of human scar transplantation was developed, but fibroblast proliferation was diminished when compared with human samples.[53] The rabbit ear excisional HSc model was developed in 1997 and has been used frequently since then to elucidate molecular pathways in HSc and testing of potential therapies.[54] Chemically induced hypertrophic scars have also been shown to occur in incisional wounds in guinea pigs.[55] In the guinea pig HSc model, glucose-6-phosphate dehydrogenase levels and histologic analysis were similar to human HSc, but HSc development was inconsistent and unpredictable between animals.

While our murine HSc model shares many characteristics with the human condition (Table 1), there are differences between mice and humans. This model does not utilize a true split-thickness skin graft because harvesting of mouse skin with a dermatome is unreliable. Additionally, the scars we observed in our model were initially flat and red, eventually becoming pale. HSc in humans are classically described as red, raised, and itchy.[27] This may be due to a diminished level of mechanical tension in the murine skin graft bed.[27,28]

HSc development is a common debilitating condition with a high morbidity and a high cost to patients, both financially and in terms of quality of life.[1–5] Several animal models have been developed to meet a growing need for modeling the pathogenesis of HSc. No model has yet to meet the criteria of a reproducible, low-cost model with adequate scientific tools that closely resembles the human pathology.[5,50] To this end, we have developed a novel, validated, immune-competent,

murine HSc contraction model which has been closely modeled after present-day burn scar conditions and management. This model possesses all of the advantages of murine models, including an abundance of genetic variants and applicable tools, low cost, and practical husbandry techniques, all of which will aid in the research and development of novel therapeutic approaches for the treatment of HSc contraction.

ACKNOWLEDGMENTS

The authors would like to thank Eugenia H. Cho for her technical assistance and Gloria Adcock for her assistance with tissue processing.

Source of Funding: This work was supported by a grant from the National Institutes of Health,K08 GM 085562-05.

Conflicts of Interest: The authors declare that there are no conflicts of interest.

REFERENCES

1. Sund B, Arrow AK. *New developments in wound care*. London: PBJ Publications, 2000: 1–255.
2. Schneider JC, Holavanahalli R, Helm P, Goldstein R, Kowalske K. Contractures in burn injury: defining the problem. *J Burn Care Res* 2006; 27: 508–14.
3. World Health Organization. *World health statistics*, 2011. Available at http://www.who.int/whosis/whostat/2011/en/ (accessed November 12, 2014).
4. Engrav LH, Garner WL, Tredget EE. Hypertrophic scar, wound contraction and hyper-hypopigmentation. *J Burn Care Res* 2007; 28: 593–7.
5. Leblebici B, Adam M, Bağiş S, Tarim AM, Noyan T, Akman MN, et al. Quality of life after burn injury: the impact of joint contracture. *J Burn Care Res* 2006; 27: 864–8.
6. Schneider JC, Holavanahalli R, Helm P, Goldstein R, Kowalske K. Contractures in burn injury: defining the problem. *J Burn Care Res* 2006; 7: 508–14.
7. Greenwood J, Amjadi M, Dearman B, Mackie I. Real-time demonstration of split skin graft inosculation and integra dermal matrix neovascularization using confocal laser scanning microscopy. *Eplasty* 2009; 9: e33.
8. Laschke MW, Menger MD. Vascularization in tissue engineering: angiogenesis versus inosculation. *Eur Surg Res* 2012; 48: 85–92.
9. Lucas T, Waisman A, Ranjan R, Roes J, Krieg T, Müller W, et al. Differential roles of macrophages in diverse phases of skin repair. *J Immunol* 2010; 184: 3964–77.
10. Converse JM, Smahel J, Ballantyne DL Jr, Harper AD. Inosculation of vessels of skin graft and host bed: a fortuitous encounter. *Br J Plast Surg* 1975; 28: 274–82.
11. Micallef L, Vedrenne N, Billet F, Coulomb B, Darby IA, Desmoulière A. The myofibroblast, multiple origins for major roles in normal and pathological tissue repair. *Fibrogenesis Tissue Repair* 2012; 5 (Suppl. 1): S5.
12. Tomasek JJ, Gabbiani G, Hinz B, Chaponnier C, Brown RA. Myofibroblasts and mechano-regulation of connective tissue remodelling. *Nat Rev Mol Cell Biol* 2002; 3: 349–63.
13. Kischer CW, Sheridan D, Pindur J. Use of nude (athymic) mice for the study of hypertrophic scars and keloids: vascular continuity between mouse and implants. *Anat Rec* 1989; 225: 189–96.
14. Escamez MJ, García M, Larcher F, Meana A, Muñoz E, Jorcano JL, et al. An in vivo model of wound healing in genetically modified skin-humanized mice. *J Invest Dermatol* 2004; 123: 1182–91.
15. Robb EC, Waymack JP, Warden GD, Nathan P, Alexander JW. A new model for studying the development of human hypertrophic burn scar formation. *J Burn Care Rehabil* 1987; 8: 371–5.
16. Wang J, Jiao H, Honardoust D, Momtazi M, Shankowsky HA, Tredget EE. Human hypertrophic scar-like nude mouse model: characterization of the molecular and cellular biology of the scar process. *Wound Repair Regen* 2011; 19: 274–85.
17. Park JE, Barbul A. Understanding the role of immune regulation in wound healing. *Am J Surg* 2004; 187: 11S–16S.
18. Aarabi S, Bhatt KA, Shi Y, Paterno J, Chang EI, Loh SA, et al. Mechanical load initiates hypertrophic scar formation through decreased cellular apoptosis. *FASEB J* 2007; 21: 3250–61.
19. Arbab MH, Dickey TC, Winebrenner DP, Chen A, Klein MB, Mourad PD. Terahertz reflectometry of burn wounds in a rat model. *Biomed Opt Express* 2011; 2: 2339–47.
20. Gould LJ, Leong M, Sonstein J, Wilson S. Optimization and validation of an ischemic wound model. *Wound Repair Regen* 2005; 13: 576–82.
21. Bond JE, et al. Angiotensin-II mediates nonmuscle myosin II activation and expression and contributes to human keloid disease progression. *Mol Med* 2011; 17: 1196–203.
22. Clark JA, Cheng JC, Leung KS. Mechanical properties of normal skin and hypertrophic scars. *Burns* 1996; 22: 443–6.
23. Varga OE, Hansen AK, Sandoe P, Olsson IA. Validating animal models for preclinical research: a scientific and ethical discussion. *Altern Lab Anim* 2010; 38: 245–8.
24. Haynes BW Jr. Early excision and grafting in third degree burns. *Ann Surg* 1969; 169: 736–47.
25. Wang J, Ding J, Jiao H, Honardoust D, Momtazi M, Shankowsky HA, et al. Human hypertrophic scar-like nude mouse model: characterization of the molecular and cellular biology of the scar process. *Wound Repair Regen* 2011; 19: 274–85.
26. Quilichini J, Benjoar MD, Hivelin M, Lantieri L. Split-thickness skin graft harvested from the scalp for the coverage of extensive temple or forehead defects in elderly patients. *Arch Facial Plast Surg* 2012; 14: 137–9.
27. Mustoe TA, et al. International clinical recommendations on scar management. *Plast Reconstr Surg* 2002; 110: 560–71.
28. McGrouther DA. Hypertrophic or keloid scars? *Eye (Lond)* 1994; 8 (Pt 2): 200–3.
29. Lupher ML Jr, Gallatin WM. Regulation of fibrosis by the immune system. *Adv Immunol* 2006; 89: 245–88.
30. Wang J, Jiao H, Stewart TL, Lyons MV, Shankowsky HA, Scott PG, et al. Accelerated wound healing in leukocyte-specific, protein 1-deficient mouse is associated with increased infiltration of leukocytes and fibrocytes. *J Leukoc Biol* 2007; 82: 1554–63.
31. Mahdavian Delavary B, van der Veer WM, van Egmond M, Niessen FB, Beelen RH. Macrophages in skin injury and repair. *Immunobiology* 2011; 216: 753–62.
32. Kischer CW, Bunce H 3rd, Shetlah MR. Mast cell analyses in hypertrophic scars, hypertrophic scars treated with pressure and mature scars. *J Invest Dermatol* 1978; 70: 355–7.
33. Hara M, Ono K, Wada H, Sasayama S, Matsumori A. Preformed angiotensin II is present in human mast cells. *Cardiovasc Drugs Ther* 2004; 18: 415–20.
34. Aarabi S, Longaker MT, Gurtner GC. Hypertrophic scar formation following burns and trauma: new approaches to treatment. *PLoS Med* 2007; 4: e234.
35. Desmouliere A, Redard M, Darby I, Gabbiani G. Apoptosis mediates the decrease in cellularity during the transition between granulation tissue and scar. *Am J Pathol* 1995; 146: 56–66.

36. Kischer CW. Fine structure of granulation tissue from deep injury. *J Invest Dermatol* 1979; 72: 147–52.
37. Hinz B, Celetta G, Tomasek JJ, Gabbiani G, Chaponnier C. Alpha-smooth muscle actin expression upregulates fibroblast contractile activity. *Mol Biol Cell* 2001; 12: 2730–41.
38. Kolodney MS, Wysolmerski RB. Isometric contraction by fibroblasts and endothelial cells in tissue culture: a quantitative study. *J Cell Biol* 1992; 117: 73–82.
39. Burridge K, Chrzanowska-Wodnicka M. Focal adhesions, contractility, and signaling. *Annu Rev Cell Dev Biol* 1996; 12: 463–518.
40. Leung T, Manser E, Tan L, Lim L. A novel serine/threonine kinase binding the Ras-related RhoA GTPase which translocates the kinase to peripheral membranes. *J Biol Chem* 1995; 270: 29051–4.
41. Chihara K, Amano M, Nakamura N, Yano T, Shibata M, Tokui T, et al. Cytoskeletal rearrangements and transcriptional activation of c-fos serum response element by Rho-kinase. *J Biol Chem* 1997; 272: 25121–7.
42. Kimura K, Fukata Y, Matsuoka Y, Bennett V, Matsuura Y, Okawa K, et al. Regulation of the association of adducin with actin filaments by Rho-associated kinase (Rho-kinase) and myosin phosphatase. *J Biol Chem* 1998; 273: 5542–8.
43. Katoh K, Kano Y, Amano M, Onishi H, Kaibuchi K, Fujiwara K. Rho-kinase–mediated contraction of isolated stress fibers. *J Cell Biol* 2001; 153: 569–84.
44. Vicente-Manzanares M, Ma X, Adelstein RS, Horwitz AR. Non-muscle myosin II takes centre stage in cell adhesion and migration. *Nat Rev Mol Cell Biol* 2009; 10: 778–90.
45. Bond JE, Ho TQ, Selim MA, Hunter CL, Bowers EV, Levinson H. Temporal spatial expression and function of non-muscle myosin II isoforms IIA and IIB in scar remodeling. *Lab Invest* 2011; 91: 499–508.
46. Wynn TA. Common and unique mechanisms regulate fibrosis in various fibroproliferative diseases. *J Clin Invest* 2007; 117: 524–9.
47. Verhaegen PD, et al. Differences in collagen architecture between keloid, hypertrophic scar, normotrophic scar, and normal skin: an objective histopathological analysis. *Wound Repair Regen* 2009; 17: 649–56.
48. Ehrlich HP, Krummel TM. Regulation of wound healing from a connective tissue perspective. *Wound Repair Regen* 1996; 4: 203–10.
49. Dunn MG, Silver FH, Swann DA. Mechanical analysis of hypertrophic scar tissue: structural basis for apparent increased rigidity. *J Invest Dermatol* 1985; 84: 9–13.
50. Ramos ML, Gragnani A, Ferreira LM. Is there an ideal animal model to study hypertrophic scarring? *J Burn Care Res* 2008; 29: 363–8.
51. Wong VW, Sorkin M, Glotzbach JP, Longaker MT, Gurtner GC. Surgical approaches to create murine models of human wound healing. *J Biomed Biotechnol* 2011; 2011: 969618.
52. Yang DY, Li SR, Wu JL, Chen YQ, Li G, Bi S, et al. Establishment of a hypertrophic scar model by transplanting full-thickness human skin grafts onto the backs of nude mice. *Plast Reconstr Surg* 2007; 119: 104–9, discussion 110–111.
53. Polo M, et al. An in vivo model of human proliferative scar. *J Surg Res* 1998; 74: 187–95.
54. Saulis AS, Mogford JH, Mustoe TA. Effect of Mederma on hypertrophic scarring in the rabbit ear model. *Plast Reconstr Surg* 2002; 110: 177–83, discussion 184–186.
55. Aksoy MH, Vargel I, Canter IH, Erk Y, Sargon M, Pinar A, et al. A new experimental hypertrophic scar model in guinea pigs. *Aesthetic Plast Surg* 2002; 26: 388–96.